This is a repository copy of *Constant envelope transceivers in millimetre-wave massive MIMO: EVM and link budget considerations*.

White Rose Research Online URL for this paper:
http://eprints.whiterose.ac.uk/133898/

Version: Accepted Version

Constant Envelope Transceivers in Millimetre-Wave Massive MIMO: EVM and Link Budget Considerations

Edward A. Ball
Communications Research Group
University of Sheffield
Sheffield, United Kingdom
e.a.ball@sheffield.ac.uk

Athanasios Vasileiadis
Communications Research Group
University of Sheffield
Sheffield, United Kingdom
avasileiadis1@sheffield.ac.uk

Abstract—RF 30 GHz ray-tracing simulation results are presented from a conceptual, Massive- Multiple Input Multiple Output (M-MIMO) propagation model in an urban canyon. The usage of Constant Envelope (CE) RF signals is evaluated in both propagation ray-rich and ray-sparse scenarios. Multiple mobile terminals are simulated, each employing single carrier Phase Shift Keying (PSK). It is found that once an operational link budget is achieved, CE transmitters have negligible effect on a received Error Vector Magnitude (EVM). Finally, it is found that the EVM is a function of both richness of propagation rays as well as the relative proximities of mobile users. A worst-case EVM of circa 25% is observed when terminals are separated by 1m, reducing to circa 5% when terminals are separated by more than 4m.

Keywords—Multiple-input-multiple-output (MIMO), massive MIMO, 30GHz, millimetre wave, ray-tracing, EVM, PSK

I. Introduction

There is now considerable research activity into the use of millimetre wave (mmWave) outdoor communications for 5G and beyond, with new channel models emerging [1]-[8]. The models are not finalised and global research activity is testing their suitability [9]-[12] and comparing to measured data. Regulators ITU and Ofcom have promoted the 26 GHz 'Pioneer Band' for 5G [13]. In parallel, Massive MIMO (M-MIMO) has been the subject of much research in low GHz bands for several years, but has only recently been considered for mmWave usage [14]-[17], in contrast to conventional phased array beam steering. This paper considers the effect of mmWave M-MIMO propagation on the signals received by a mobile RF device. The aim is to identify future simplification opportunities for mmWave RF hardware for mobile applications. Given the complexity, power consumption and cost of mmWave radio hardware, it is vitally important to research ways of simplifying future RF hardware implementation. There has so far been limited research into the hardware architectural implications of M-MIMO using non-ideal RF components and subsystems [18]-[20]; with researchers often using idealised models of the channel (independent, identically distributed). There is insufficient published measured propagation data for mmWave mobile scenarios, or data relevant to mmWave M-MIMO use-cases. This paper addresses this lack of data via a simple analytical model and presents simulation findings from three single-antenna mobile User Equipment (UE) terminals simultaneously receiving in a mmWave M-MIMO system. Composite multiple PSK symbols are compressed to CE, prior to transmission by RF Power Amplifiers (PAs) at each MIMO radiating element. Such an approach would thus support the use of high efficiency RF PAs, since the transmitted signal would not contain amplitude modulated components.

A ray tracing [21], geometric model of a city street was used to create both rich and sparse reflection channel models. The channel models were used to evaluate the individual ray tracing component rays transmitted from Base Station (BS) radio antenna elements and received by each single-antenna UE. Various BS array sizes have been investigated. The composite signal was analysed for receiver (RX) constellation symbol EVM and RX signal level. Each M-MIMO BS element's conducted transmit (TX) power was set to +10dBm, representing pragmatic hardware capability for single chip transceivers. Each BS to UE downstream transmission shared an equal proportion of the BS TX power. The BS antennas formed a Uniform Rectangular Array (URA) of grid N elements by N elements (NxN). The antenna elements at the BS and UE were simple patch antennas, with assumed 0 dBi gain and uniform coverage in the direction of transmission; similar to approaches in [15].

The contributions of this paper are 1) proposal of model for predicting the number of diffuse rays from a rough surface at mmWave. 2) Discovery of EVM dependency on relative UE spacing 3) Discovery of link budget requirement being limiting factor, rather than EVM, for mmWave mobile operation.

II. Simulation Model

A. mmWave Reflection Model for Ray Tracing

The modelled 30 GHz urban street scenario consisted of concrete buildings lining an asphalt road, forming an urban canyon. Simulations at mmWave must include effects of the

building material [22]. The simulation parameters were: asphalt road & pavement combined width is 10 m (relative permittivity ε_r is 3.2-j0.1, conductivity σ is 0.1 mS/m); canyon concrete wall relative permittivity ε_r is 6.2-j0.4 & conductivity σ is 0.1 mS/m; M-MIMO BS URA antenna element grid spacing is 1 cm; height of UE is 1 m; height of BS is 10 m; concrete and asphalt peak surface roughness is 1 cm (due to use of aggregate stones of edge 1 cm). Surface reflections were assumed to be diffuse (since wavelength is comparable to surface roughness), hence requiring modelling of multiple reflected rays. The magnitude of the reflection coefficient Γ for a ray intercepting a surface was calculated via wave impedances, using (1).

$$|\Gamma| = \left|\frac{Z_2 - Z_1}{Z_2 + Z_1}\right| \qquad (1)$$

The parallel, or perpendicular, incident angle (θ_i) and transmitted angle (θ_t) dependent surface impedances are defined as follows [8]:-

$$Z_{2\_parrallel} = \eta_2 \cos\theta_t \qquad (2a)$$
$$Z_{2\_perpendicular} = \frac{\eta_2}{\cos\theta_t} \qquad (2b)$$
$$Z_{1\_parallel} = \eta_1 \cos\theta_i \qquad (3a)$$
$$Z_{1\_perpendicular} = \frac{\eta_1}{\cos\theta_i} \qquad (3b)$$

The wave impedance of air is $\eta_1 = 120\pi$ and for the reflecting medium (concrete or asphalt) is η_2:

$$\eta_2 = \sqrt{\frac{j\omega\mu}{\sigma + j\omega\varepsilon}} \qquad (4)$$

The value of θ_t was computed for each ray, by application of Snell's law and knowing the angle of ray incidence θ_i [23],

$$sin(\theta_t) = \frac{\gamma_1}{\gamma_2} sin(\theta_i) \qquad (5)$$

where $\gamma_{1,2} = \frac{-\omega\mu}{j\eta_{1,2}}$, ω is the carrier frequency in radians/s, $\mu = \mu_r\mu_0 = 4\pi 10^7$ H/m and $\varepsilon = \varepsilon_0\varepsilon_r = \varepsilon_r 8.85 * 10^{-12}$ F/m.

The phase of the reflected rays was assumed to be random, due to the surface roughness being comparable to wavelength.

B. Estimation of Number of mmWave Reflected Rays

The canyon street model of the ray tracing simulation for 1 UE, is shown in Fig. 1. Rays F1 & F2 represent example road floor reflections from the glistening area. Rays S1 & S2 are example single wall reflections from glistening on the concrete walls W1 & W2. Rays D1 & D2 are example double-wall reflection rays from walls W1 & W2. All rays are modelled travelling from BS to UE.
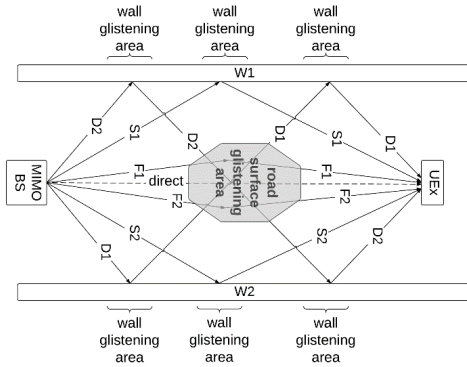

Fig. 1. Plan view of canyon ray-tracing scenario with 1 UE.

The number of contributing reflecting rays was predicted based on the likelihood of an individual component ray from a BS TX element intercepting an appropriately orientated reflecting stone and the resulting reflected ray then intercepting the UE RX. The reflecting objects are aggregate stones within the illuminated surface *glistening area*. The size of the glistening area for rough surfaces is often assumed to be the 1st Fresnel Zone projected on the ground [24]. However, since the stones in the road (or wall) surface were comparable to the 30 GHz wavelength it was decided for this scenario that a geometric model was required, which considered a larger potential reflecting area. The geometric model was used to calculate the maximum area of glistening zone that could support a reflection from BS TX to UE RX. A stone's reflecting surface 2 dimensional orientation (pitch and yaw) was limited by rotation; defined as a *peak facet angle* [24]. The glistening area size can be calculated based on the peak facet angle and the heights of BS and RX antennas.

The total number of rays emerging from the road surface glistening zone, of area *GA*, consisting of many stones of individual surface area *SA* and with probability of a stone being correctly orientated in pitch axis $P(S_P)$ and correctly orientated in yaw axis $P(S_Y)$, is given by (6):

$$N_{road} = \frac{GA}{SA}.P(S_P).P(S_Y) \qquad (6)$$

The probability of a stone being in the correct pitch and yaw angular position is dependent on the tolerable rotational angle that would lead to the front surface of the resulting reflected ray cone intercepting the UE RX antenna. This can be approximated by simple geometry, based on the size of the stone and its distance from the UE RX antenna:

$$P(S_P) = \frac{\zeta_V}{2.PeakFacetAngle} \qquad (7)$$
$$P(S_Y) = \frac{\zeta_H}{2.PeakFacetAngle} \qquad (8)$$

where, the tolerable pitch and yaw angle ranges are defined by:

$$\zeta_V = arctan\left(\frac{h_r + 2r}{d_2}\right) - arctan\left(\frac{h_r}{d_2}\right) \qquad (9)$$
$$\zeta_H = 2.arctan\left(\frac{r}{d_2}\right) \qquad (10)$$

The radius of the ray cone beam r at the RX location is:

$$r = \sqrt{\frac{SA.d^2}{\pi(d - d_2)^2}} \qquad (11)$$

where h_r is the vertical height of RX antenna, d_2 is the horizontal distance from the centre of the glistening zone to RX, and d is the horizontal distance between BS TX and UE RX.

The same approach was used to estimate the number of rays due to reflections from a glistening zone on a single wall. For double wall reflections (i.e. ray bounce across road and back) each wall had a glistening zone, with the number of rays estimated based on the probability of stones in both surfaces being fortuitously aligned to pass rays from BS TX to UE RX.

The number of reflected rays is a function of the stones' peak facet angle in pitch and yaw (for example, varying the peak facet angle from 10 degrees to 40 degrees led to a reduction in the number of road reflections from 13 to 7 rays). The simulations reported here used a 10 degree peak facet angle.

Simulations predicted a ray-rich set (per each direct ray) consisting of: 13 rays from road reflections, 8 rays from single wall reflections and 10 rays from double wall reflections. This is comparable to the overall number of rays from multiple time cluster sub-paths being proposed in other channel models [2]. However, it is recognised that reduced ray sets are more likely, so simulation results are also presented for ray-sparse reflection. The ray-sparse set for each M-MIMO BS element was defined as: 4 rays from road reflections, 2 rays from single wall and 2 rays from double wall reflections, for any BS antenna element. This set of 8 total reflected rays is closer to the 5 to 7 ray models now often used by other researchers [9], [14], [21], [25].

C. M-MIMO Channel Simulation Model

Early investigations using the propagation model showed that the RMS delay spread for the canyon scenario was circa 10ns at 150m distances (coherence bandwidth circa 100MHz). Given the simplicity of the model, the delay spread is plausible compared to values others have reported over similar distances: 29.9ns [25], 32ns [26], 32ns [9], 22.3ns [11]. Using a modulation bandwidth (BW) less than the coherence BW allows use of a simple flat-fading gain-phase channel model. This was then used to represent the channel transfer characteristic between each of the URA elements at the BS and a UE. This valuable simplification permits a simple channel model based on ray geometry to be created: capturing the effects of multiple rays and their reflections, from an element in the NxN BS array to the UE.

D. M-MIMO Precoding at the BS

The three UE channel gain-phase responses ($H_{UE1}, H_{UE2}, H_{UE3}$) were then used for calculating MIMO BS TX precoding coefficients for the UEs. A Matched Filter (MF) [27], consisting of the conjugate of the channel response, was used for MIMO channel precoding of BS data TX symbols:

$$W_{UE1,2,3} = \frac{H^*_{UE1,2,3}}{mean(H_{UE1,2,3})} \qquad (12)$$

where * denotes the complex conjugate of each element. Usage of this model therefore mandates the simplifying assumption that the channel response does not change over the subsequent symbol interval. The MF precoding was chosen as it is low-complexity, which is important when considering the DSP computing resource that will be required for practical implementations of very large array M-MIMO base stations.

E. Constant Envelope Transmitter Model

Random sets of PSK TX symbols $S_{UE1}, S_{UE2}, S_{UE3}$ were created for sending to the three UEs. The symbols were precoded and then combined, for multi-user transmission, by each BS TX element. The URA NxN composite TX signal amplitude with TX power Pt is (50 ohm system):

$$T_{composite} = (W_{UE1}S_{UE1} + W_{UE2}S_{UE2} + W_{UE3}S_{UE3})^2\sqrt{50Pt} \quad (13)$$

The composite signal was then passed through a model of the BS CE PAs, for all NxN BS TX elements as per (14). No precoding adaptions were made to accommodate the CE TX (as considered by other researchers [28]).

$$T_{CE}[x,y] = \frac{T_{composite}[x,y]}{|T_{composite}[x,y]|}\sqrt[2]{50Pt} \qquad (14)$$

In (14), *x* & *y* define the URA BS array TX antenna element grid position, which would each have an associated TX CE PA.

The signal received at a particular UE was modelled as the vector sum of signals from all composite BS elements, with associated channel gain-phase response. The model produced the resultant UE RX antenna output for both Variable Envelope (VE) TX defined by (15) and for the CE TX defined by (16):

$$R_{VE1,2,3} = \sum_x \sum_y H_{UE1,2,3}[x,y]T_{composite}[x,y] \quad (15)$$

$$R_{CE1,2,3} = \sum_x \sum_y H_{UE1,2,3}[x,y]T_{CE}[x,y] \qquad (16)$$

$R_{VE1,2,3}$ and $R_{CE1,2,3}$ are the complex amplitudes of the received symbol constellation at the RX antenna output for UE1, UE2 and UE3: hence allowing the EVM and link budget to be evaluated. Multiple simulation runs were performed, each generating new channel gain-phase responses and TX symbols, thus allowing averages of results to be obtained.

III. RESULTS OF SIMULATION AND DISCUSSION

Table I shows the RX signal power and RX EVM due to interference from the other UEs, for the ray-rich propagation model. Table I shows the performance as a function of BS URA size for both CE and VE TX transmissions. (URA array size is defined as array length N multiplied by array width N.)

UE RX sensitivity was predicted based on single carrier, offset-QPSK modulation, with an RX system Noise Figure of 12 dB and with the full coherence BW of each UE used for symbol transmission. The coherence BW was calculated based on the RMS delay spread observed by each UE. In the ray-rich scenario of Table I, the coherence BWs were calculated to be 130 MHz for UE1, 250 MHz for UE2 and 498 MHz for UE3 (distances are given in the table.) The resulting RX sensitivities were UE1: -70 dBm, UE2: -67 dBm and UE3: -64 dBm. Therefore, assuming subsequent implementation of BS TX power balancing, the 64x64 (i.e. 4096 element URA) BS array is the smallest offering sufficient link budget for all UEs in the ray-rich scenario.

From Table I, the EVM of the 16x16 BS array was below 5 % but required the BS element TX powers to be increased to +34 dBm to meet the link budget sensitivity requirements.

TABLE I
EVM & RX POWERS FOR UEs VARIOUSLY SPACED FROM BS
{RAY-RICH CHANNEL, UE1 AT 50 M, UE2 AT 100 M, UE3 AT 200 M FROM BS}

BS URA array size	UE1 EVM VE / CE (%)	UE2 EVM VE / CE (%)	UE3 EVM VE / CE (%)	UE1 RX level (dBm)	UE2 RX level (dBm)	UE3 RX level (dBm)
64x64	1.4/1.5	1.3/1.5	1.2/1.4	-51	-58	-68
51x51	1.4/1.7	2/2	1.9/2.2	-59	-66	-75
32x32	2.1/2.4	3.4/3.5	3.3/3.2	-75	-82	-92
16x16	3.8/4.6	4.1/5.2	4.4/3.9	-99	-106	-116
8x8	12/16	10/12	10/14	-123	-130	-140

It is proposed that +34 dBm conducted TX power would be impractical for low-cost RF hardware based on single chip transceivers. Hence, the 64x46 array would be pragmatic to serve the 3 UEs at the quoted distances, using 10 dBm TX stages. The simulation was also run with the ray-sparse scenario, with UE distances again as per Table I. An 86x86 array was now the minimum size able to meet the UE sensitivities at the quoted BS distances; also providing an EVM below 1.5 %.

The model was then used to predict the EVM as a function of array size in both ray-rich and ray-sparse scenarios when the 3 UEs are grouped close to the BS (Fig. 2 and Fig. 3). Both Fig. 2 and Fig. 3 show that once the array size is larger than 20x20 there is negligible difference in EVM between UEs, or as a function of CE or VE TX usage. However, to achieve the coherence bandwidth defined link budgets at the quoted distances in Fig. 2 and Fig. 3 required a minimum URA size of 32x32 minimum (1024 elements).
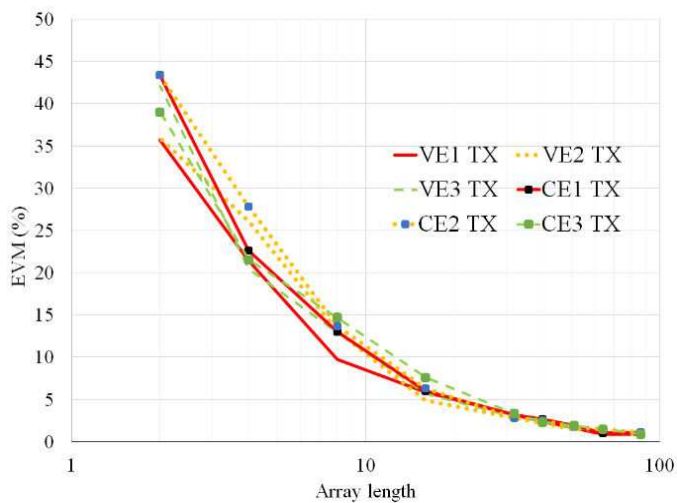

Fig. 2. EVM as function of one dimensional array size N (UE 1 at 20 m, UE2 at 30 m, UE3 at 30 m), ray-rich model.
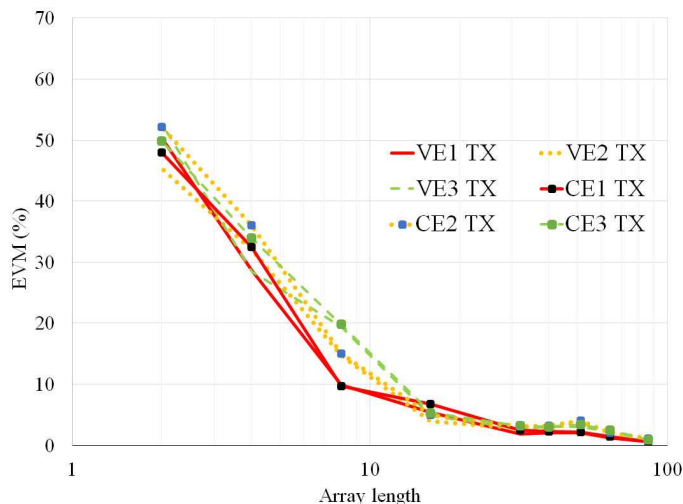

Fig. 3. EVM as function of one dimensional array size N (UE 1 at 20 m, UE2 at 30 m, UE3 at 30 m), ray-sparse model.
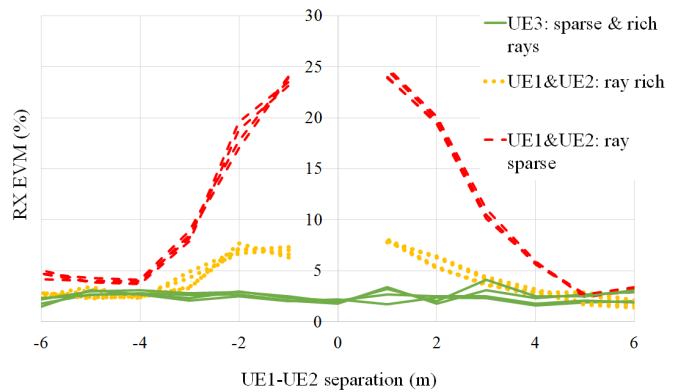

Fig. 4. EVM as function of UE1-UE2 separation (circa 40 m from BS), UE3 70 m from BS (BS array size 39x39 = 1521 elements). VE and CE data shown.

Fig. 4 shows UE1 and UE2 RX EVM as a function of their mutual separation, for both VE and CE TX (note, negligible additional effects are seen due to usage of CE TX). Fig. 4 also shows results for both the rich and sparse ray sets. It is clear the EVM improves significantly as the adjacent UEs separate by only a few meters.

From the collected figures above, there is an obvious EVM degradation when fewer reflected rays are present; but it is only high when UEs are adjacent and is also a function of their distance to the BS. Importantly, there is negligible difference in EVM between CE and VE TX. (An EVM of below 5 % is often considered acceptable in RF systems.)

IV. CONCLUSION

From the simulations performed, some initial M-MIMO mmWave RF architectural implications can be identified: **1)** In a PSK system with a large BS array concurrently serving 3 UEs, RX EVM is not a strong function of CE TX. This is due to the overriding need for sufficient BS TX elements to meet UE RX sensitivity at useful outdoor range (i.e. > 20 m), exceeding the number of elements required for low EVM alone. **2)** RX EVM is a function of relative proximity of UEs, UE to BS distance and propagation ray 'richness'. This implies a pragmatic mmWave M-MIMO modulation scheme should be adaptive (i.e. able to tolerate EVMs from 5 % to circa 30 %) and could be based on single carrier PSK symbol modulation, with low complexity MF conjugate precoding for CE TX chains with efficient PAs. **3)** A mmWave UE at 200 m from the BS can be supported, by appropriate BS array sizing and BS TX power control & sharing. Explicit forming and pointing of a single narrow beam does not appear to be a prerequisite for mmWave communications. **4)** Due to the large number of BS array transceiver elements (1 per BS antenna), mmWave M-MIMO BS hardware architectures should focus on low DC power, cost-effective hardware solutions, with attendant simple baseband implementations. **5)** A dynamically configurable BS array size will allow a run-time trade-off between numbers of UEs supported, service range and DC power draw.

Overall, it is anticipated that the work in this paper could now lead to significant new research into mmWave RF hardware architectures and circuit implementations for future energy efficient mmWave mobile radio systems.

References

[1] T. S. Rappaport, G.R. MacCartney, M. K. Samimi, and S. Sun, "Wideband millimeter-wave propagation measurements and channel models for future wireless communication system design," *IEEE Trans. on Communications*, vol. 63, no. 9, pp. 3029-3056, May 2015.

[2] T. A. Thomas, H.C. Nguyen, G.R. MacCartney, and T. S. Rappaport, "3D mmwave channel model proposal," in *Vehicular Technology Conference*, Vancouver, B.C., Sept. 2014, pp. 1-6.

[3] ITU, ITU-R 1411-9, [Online]. Available: https://www.itu.int/rec/R-REC-P.1411-9-201706-I/en.

[4] METIS, "Mobile and wireless communications enablers for the twenty-twenty information society, D1.4, METIS Channel Models," 2015, [Online]. Available: http://www.metis2020.com.

[5] 3rd Generation Partnership Project (3GPP), "Study on channel model for frequency spectrum above 6GHz, TR 38.900 V14.2.0," Dec. 2016.

[6] mmMagic, "mm-wave based mobile radio access network for 5G integrated communications, W2.1, 6-100GHz channel modelling for 5G: measurement and modeling plans in mmMAGIC," 2016, [Online], Available: https://5g-mmmagic.eu.

[7] MiWEBA, "Millimetre-wave evolution for backhaul and access, D5.1, channel modeling and characterization," 2014, [Online], Available: http://www.miweba.eu.

[8] 3GPP. "Study on channel model for frequency spectrum above 6GHz, TR 38.900," Sep. 2016. [Online]. Available: http://www.3gpp.org.

[9] X. Zhao, S. Li, Q. Wang, M. Wang, S. Sun, and W. Hong, "Channel measurements, modeling, simulation and validation at 32GHz in Outdoor Microcells for 5G radio systems," *IEEE Access*, vol. 5, pp. 1062-1072, March 2017.

[10] T. S. Rappaport, S. Sun, and M. Shafi, "Investigation and comparison of 3GPP and NYUSIM channel models for 5G wireless communications," in *IEEE Vehicular Technology Conference (VTC-Fall)*, Toronto, Canada, Sept. 2017, pp. 1-5.

[11] S. Hur, Y-J. Cho, T. Kim, J-H. Park, A. F. Molisch, K. Haneda, and M. Peter, "Wideband spatial channel model in urban cellular environments at 28GHz," in *2015 9th European Conference on Antennas and Propagation (EuCAP)*, Lisbon, Portugal, April 2015, pp. 1-5.

[12] J. Lee, M-D. Kim, J. Liang, J-J. Park, and B. Park, "Frequency range extension of the ITU-R NLOS path loss model applicable for urban street environments at 28GHz measurements," in *10th European Conference on Antennas and Propagation (EuCAP)*, Davos, Switzerland, April 2016, pp. 1-5.

[13] Ofcom, "5G spectrum access at 26 GHz and update on bands above 30 GHz," [Online] Available https://www.ofcom.org.uk/__data/assets/pdf_file/0014/104702/5G-spectrum-access-at-26-GHz.pdf.

[14] H. Zhang, S. Venkateswaran, and U. Madhow, "Channel modelling and MIMO capacity for outdoor millimeter wave links," in *Wireless Communications and Networking Conference (WCNC)*, Sydney, NSW, April 2010, pp. 1-6.

[15] J. Lota, S. Sun, T. S. Rappaport, and A. Demosthenous, "5G uniform linear arrays with beamforming and spatial multiplexing at 28, 37, 64, and 71 GHz for outdoor urban communications: a two-level approach," *IEEE Trans. on Vehic. Tech.*, vol. 66, no. 11, pp. 9972-9985, November 2017.

[16] C. T. Neil, M. Shafi, P.J. Smith, P.A. Dmochowski, and J. Zhang, "Impact of microwave and mmWave channel models on 5G system performance," *IEEE Trans. on Antennas and Propagation*, vol. 65, no. 12, pp. 6505-6520, Dec. 2017.

[17] J. Huang, C-X. Wang, R. Feng, W. Zhang, and Y. Yang, "Multi-frequency mmWave massive MIMO channel measurements and characterization for 5G wireless communications systems," *IEEE Journal on Selected Areas in Communications*, vol. 35, no. 7, pp. 1591-1605, July 2017.

[18] S. K. Mohammed, and E. G. Larsson, "Per-antenna constant envelope precoding for large multi-user MIMO systems," *IEEE Trans. on Communications*, vol. 61, no. 3, pp. 1059-1071, Feb. 2013.

[19] E. Bjornson, J. Hoydis, M. Kountouris, and M. Debbah, "Massive MIMO systems with non-ideal hardware: energy efficiency, estimation and capacity limits," *IEEE Trans. on Information Theory*, vol. 60, no. 11, pp. 7112-7139, Sept. 2014.

[20] Y. Wu, Y. Gu, and Z. Wang, "Channel estimation for mmWave MIMO with transmitter hardware impairments," *IEEE Communications Letters*, vol. 22, no. 2, pp. 320-323, February 2018.

[21] J-H. Lee, J-S. Choi, and S-C. Kim, "Cell coverage Analysis of 28GHz millimeter wave in urban microcell environment using 3-D ray tracing," *IEEE Trans. on Antennas and Propagation*, vol. 66, no. 3, pp. 1479-1487, March 2018.

[22] J-H. Lee, J-S. Choi, J-Y. Lee, and S-C. Kim, "Permittivity effect of building materials on 28GHz mmWave channel using 3D ray tracing simulation," in *GLOBECOM 2017 - 2017 IEEE Global Communications Conference*, Singapore, Singapore, Dec. 2017, pp. 1-6.

[23] Y. Huang and K. Boyle, *"Field concepts and radio waves,"* in *Antennas From Theory To Practice,* 1st ed., Chichester, UK, Wiley, 2008, ch. 3, sec. 3.2, pp. 80-85.

[24] R. M. Narayanan, D. D. Cox, J. M. Ralston, and M. R. Christian, "Millimeter-wave specular and diffuse multipath components of terrain," *IEEE Trans. on Antennas and Propagation*, vol. 44, no. 5, pp. 627-645, May 1996.

[25] M. K. Samimi, and T. S. Rappaport, "Local multipath model parameters for generating 5G millimeter-wave 3GPP-like channel impulse response," in *the 10th European Conference on Antennas and Propagation*, Davos, Switzerland, April 2016, pp. 1-5.

[26] M. K. Samimi, and T. S. Rappaport, "3-D statistical channel model for millimeter-wave outdoor mobile broadband communications*,"* in *2015 IEEE International Conference on Communications (ICC)*, London, UK, June 2015, pp. 2430-2436.

[27] L. Lu, G. Y. Li, A. L. Swindlehurst, A. Ashikhmin, and R. Zhang, "An overview of massive MIMO: benefits and challenges," *IEEE Journal of Selected Topics in Signal Processing*, vol. 8, no. 5, pp 742-758, April 2014.

[28] J-C. Chen, C-K. Wen, and K-K. Wong, "Improved constant envelope multiuser precoding for massive MIMO systems," *IEEE Communications Letters*, vol. 18, no. 8, pp. 1311-1314, July 2014.